RESEARCH ARTICLE | FEBRUARY 18 2025

Giant second harmonic generation in two-dimensional tellurene with synthesis and thickness engineering

Boqing Liu ; Kun Liang; Qingyi Zhou ; Ahmed Raza Khan ; Zhuoyuan Lu ; Tanju Yildirim ; Xueqian Sun ; Sharidya Rahman ; Yun Liu ; Zongfu Yu ; Yuerui Lu

Appl. Phys. Rev. 12, 011414 (2025)
https://doi.org/10.1063/5.0218276

Applied Physics Reviews ARTICLE pubs.aip.org/aip/are

Giant second harmonic generation in two-dimensional tellurene with synthesis and thickness engineering

Cite as: Appl. Phys. Rev. **12**, 011414 (2025); doi: 10.1063/5.0218276
Submitted: 10 May 2024 · Accepted: 13 January 2025 ·
Published Online: 18 February 2025

Boqing Liu,[1] Kun Liang,[1] Qingyi Zhou,[2] Ahmed Raza Khan,[1,3] Zhuoyuan Lu,[1] Tanju Yildirim,[4] Xueqian Sun,[1] Sharidya Rahman,[1,5] Yun Liu,[6] Zongfu Yu,[2] and Yuerui Lu[1,7,a)]

AFFILIATIONS

[1]School of Engineering, College of Engineering, Computing & Cybernetics, The Australian National University, Canberra, ACT 2601, Australia
[2]Department of Electrical and Computer Engineering, University of Wisconsin-Madison, Madison, Wisconsin 53706, USA
[3]Department of Industrial and Manufacturing Engineering, University of Engineering and Technology Lahore (Rachna College Campus), Gujranwala 54700, Pakistan
[4]International Center for Young Scientists (ICYS), National Institute for Materials Science (NIMS), 1-1 Namiki, Tsukuba, Ibaraki 305-0044, Japan
[5]Department of Materials Science and Engineering, Monash University, Clayton, VIC 3800, Australia
[6]Research School of Chemistry, College of Science, The Australian National University, Canberra, ACT 2601, Australia
[7]ARC Centre of Excellence in Quantum Computation and Communication Technology ANU Node, Canberra, ACT 2601, Australia

[a)]**Author to whom correspondence should be addressed:** yuerui.lu@anu.edu.au

ABSTRACT

Second harmonic generation (SHG) is a prominent branch of non-linear optics (NLO) heavily reliant on conventional bulk NLO crystals. However, the difficulty in downsizing these crystals imposes technical limitations on the future of miniaturized NLO devices. Tellurene emerges as a promising candidate to overcome these restrictions, excelling in electrical applications and believed to possess a giant second-order optical susceptibility comparable to conventional NLO crystals. In this study, a face-to-face substrate configuration is employed for the synthesis of ultrathin tellurene via PVD. Our findings reveal that tellurene's SHG performance surpasses that of monolayer transition metal dichalcogenides by two orders of magnitude, with maximum efficiency when the flake thickness is between 16 and 20 nm under various wavelengths. High sensitivity to thickness variation encourages post-growth thinning through hydrogen plasma etching, enabling precise engineering of the flake thickness for optimal SHG. This establishes a foundation for controlled tellurene thickness, further broadening its potential in diverse applications.

Since the discovery of graphene, intensive investigations into two-dimensional (2D) group III and V single-element transition metals, including borophene,[1] silicene,[2] germanene,[3] phosphorene,[4] and antimonene,[5] have gained significant momentum, due to their promising semi-metallic and semiconducting properties.[6] In 2017, 2D tellurium known as tellurene with a crystal structure consisting of atomic helical chains that spiral along one of the axes of the crystal lattice was successfully fabricated.[7,8] Bulk phase tellurium (Te) possesses intriguing properties including semiconducting capabilities,[9,10] photoconductivity,[11] thermoelectricity,[12] and piezoelectricity,[13] which are widely used in electronics, sensors, optoelectronics, and energy devices. Tellurene not only well preserves these merits in its two-dimensional form,[14] but also exhibits extraordinary carrier mobility,[15] environmental stability,[16] and low thermal conductivity,[17] when compared to other 2D materials, such as transition metal dichalcogenides (TMDCs) and black phosphorus (BP).[6,18,19] Tellurene's intrinsic nanoscale properties demonstrate potential for high-performance nano- and micro-devices, including field-effect transistors,[20] Peltier coolers,[21] and quantum Hall effect devices.[22] Moreover, tellurene's versatile optical properties signify its potential as an outstanding candidate in future optical devices. For example, the exceptional light absorption of tellurene in the mid-infrared and infrared range offers a platform for the development of

future photonics, such as photodetectors.[23–25] Meanwhile, given the wideband nonlinear saturation absorption and strong light–matter interaction from the visible to infrared range, nonlinear photonic devices based on tellurene can function as a saturable absorber,[26] photonic diode, and all-optical switcher.[27]

Second harmonic generation (SHG) is a crucial nonlinear optical (NLO) process observed in crystals, where intense optical pumping converts energy into light with double its frequency, playing a key role in frequency conversion for laser and imaging technology applications.[28] SHG studies in 2D materials are expected to make significant contribution to the ongoing trend of miniaturization in optical devices, offering potential solutions to the limitations associated with conventional bulk materials like lithium niobate ($LiNbO_3$).[29] However, among known 2D materials, some stable candidates exhibit relatively weak SHG and require NLO modulation strategies to enhance performace,[29–32] while others demonstrate strong SHG potential but are prone to degradation in ambient conditions, such as GaSe[33] and $NbOI_2$.[34] These factors significantly influence the reliability and endurability of their sustained and robust SHG performance in practical applications. In previous studies, tellurene has been experimentally proven to have robust piezoelectricity in ambient conditions,[35] and it is theoretically believed to possess a giant second-order coefficient χ^2 owing to its broken inversion symmetry in the unique helical chain structure.[36,37] Despite the anticipated potential of 2D telluride (tellurene) to serve as promising candidates for novel SHG emitters, there remains a lack of comprehensive studies experimentally elucidating its SHG performance.

In this work, extraordinary SHG performance under various excitation wavelengths has been experimentally observed from tellurene flakes, which are fabricated using the confined zone substrate configuration via the physical vapor deposition (PVD) method. This method effectively promotes a higher yield of high-quality tellurene flakes thinner than 30 nm, compared to other vapor deposition methods. Comprehensive SHG measurements reveal that the intensity of tellurene flakes easily surpasses TMD monolayer films, by up to two orders of magnitude, and moreover, the emission efficiency is highly sensitive to the flake thickness and excitation wavelength. The hydrogen plasma etching was thus adopted as the post-growth thinning process to realize modulation of the sample thickness, where the processed tellurene samples with the well-preserved crystallinity consistently exhibit robust SHG performance across a range of excitation wavelengths. These results emphasize the exceptional performance and potential of tellurene in nonlinear optics, while also highlighting the significant implications of our methods for the production and processing of tellurene in future applications.

PVD is widely unutilized to synthesize high-quality single crystal films. Compared to the traditional way to place the substrate in PVD methods for tellurene production, this work uses a face-to-face contact stacked substrate configuration and ultrahigh vacuum condition to successfully produce tellurene flakes [Fig. 1(a)]. The high purity Te precursor and stacked substrates are placed in the heating zone and growth zone near the insulation region prior to the growth procedure. An appropriately set distance between the heating and growth zones, coupled with proper pumping down procedures, synergistically contributes to the efficient deposition temperature for producing thin 2D flakes (Supplementary material). With an increase in temperature, and the application of a vacuum, the solid Te precursor vaporizes and converts into Te molecules, which then can transfer into the narrow space between substrates, finally depositing onto the bottom substrate [Fig. 1(b)]. During this process, appropriate temperature and time empower Te molecules to overcome the formation energy barrier, enabling lateral movement for the van der Waals epitaxy.[38] Consequently, Te forms covalent bonds in a helical chain configuration, primarily aligned along the $[000\,\bar{1}]$ direction, where this initial bonding arrangement triggers the growth of Te nanowires (1D), followed by the epitaxial growth in lateral and vertical directions, manifesting in the formation of tellurene flakes [Figs. 1(b) and 1(c)]. Stacking substrates appear to provide a confined-growth space configuration, remarkably stabilizing the flow rate between substrates, which establishes a controllable growth environment for yielding thin flakes.[39–41] While pumping down, the gas flow velocity outside of the confined space is further increased to effectively lower deposition and crystallization temperature, which is crucial for tellurene's morphological evolution.[24,42,43] Hence, the vacuum conditions and the arrangement of stacked substrates play vital roles in modulating the relevant growth energies and kinetics, contributing favorably to the formation, yield, and uniformity of thin tellurene flakes [Fig. 1(d)]. Taking advantage of this method, we find that more than half of the tellurene flakes are thinner than 35 nm, and around 31% of the could be as thin as 25 nm [Fig. 1(e)], which is significantly larger yield compared to single crystal thin flakes (<50 nm) fabricated by other vapor deposition methods,[24,38,42,43] and is comparable to the products of solution synthesis methods.[20] Raman tests, encompassing investigations into thickness, angle, and temperature dependencies, were conducted (supplementary material Note 2 and Figs. S1–S3), which strongly reaffirm the high purity and crystalline quality of the synthesized tellurene, consistent with earlier findings in the literature.[17,20,24,44]

Tellurene is believed to possess great potential for SHG, doubling frequency of excitation light, owing to its helical chain structure and non-centrosymmetric crystal structure [Fig. 2(a)].[36,45] To confirm SHG properties, a tellurene flake was examined with a laser source at a wavelength of 900 nm in response to varying excitation powers. The results demonstrate that the emission intensity became stronger as the excitation power increased, which is described by a linear relationship with a fitting slope value approximately equal to 2.01 [Fig. 2(b)]. This indicated that the emission intensity is proportional to the square of the power of the laser beam, complying with the SHG principle,[31,45–48] further elucidating the SH emission of tellurene. In Fig. 2(c), a quick comparison has been conducted between the tellurene flake and transition metal dichalcogenide (TMD) materials, known for their robust SHG potential. Under identical excitation conditions, tellurene exhibits a substantial SHG signal, surpassing the signal strength of various monolayer TMD flakes by nearly 100-fold. Moreover, it even outperforms the SHG signal of similarly thick MoS_2 with rhombohedral stacking by an order of magnitude. The extraordinary performance observed in tellurene is attributed to its giant second-order nonlinear susceptibility, which is two orders of magnitude larger than that of the conventional nonlinear optical (NLO) crystal $LiNbO_3$, and nearly twice as large as that of another 2D NLO crystal, 3R-MoS_2 (Fig. S4). Such high second-order nonlinear susceptibility is arisen from the unique lattice structure, where 2D flake is formed by stacking of triple helix chain via van der Waals force. The quasi-one-dimensional structures exhibit directional covalent bonding resulting in large optical matrix elements and large joint DOS for large $\chi(2)$ values.[49,50]

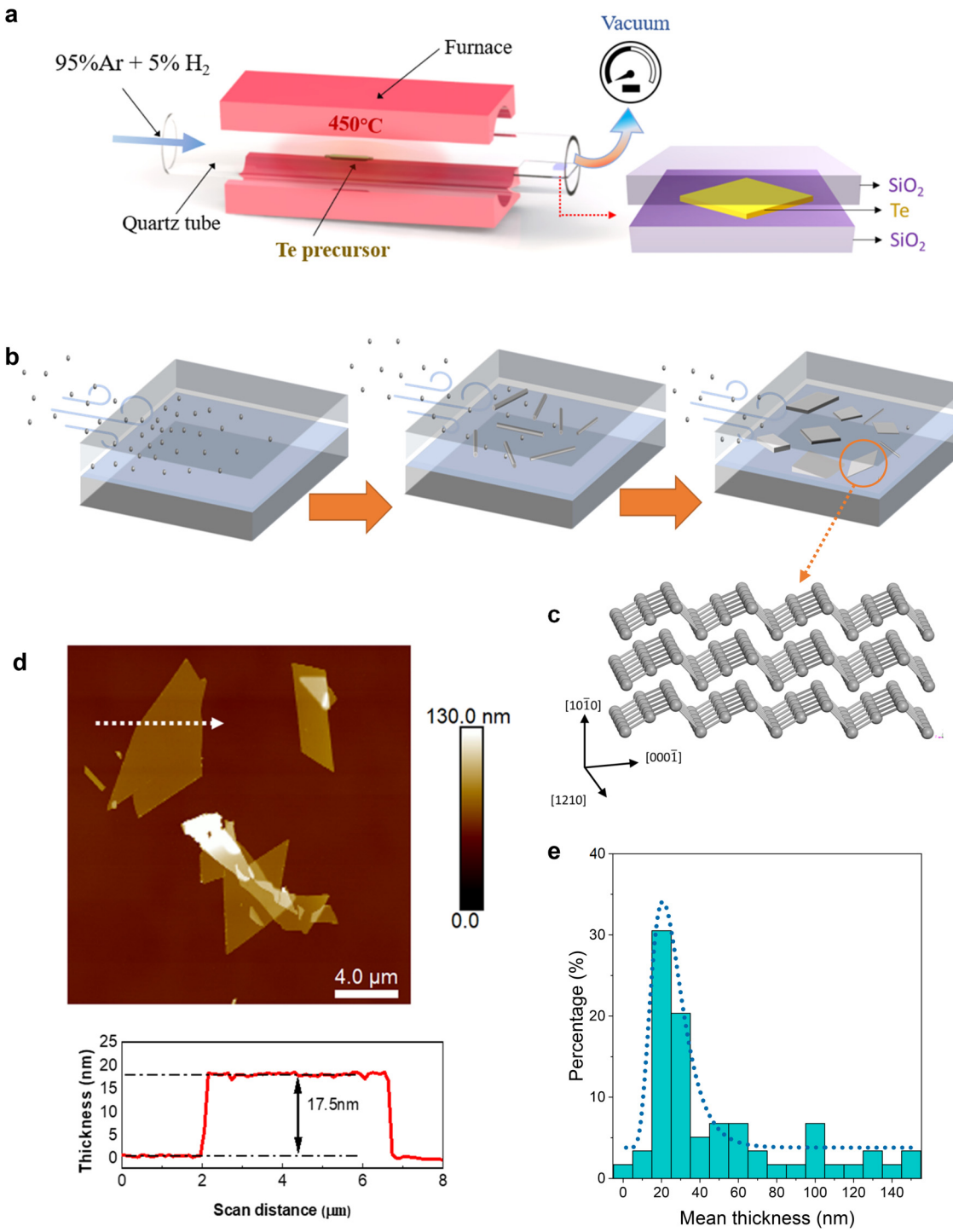

FIG. 1. Two-dimensional tellurene crystals synthesized with PVD method. (a) Schematic of tellurene flakes grown using the PVD method with a face-to-face contact substrate configuration under vacuum conditions. The face-to-face contact substrate is depicted in the inset. (b) Schematic diagram of the growth mechanism and morphologic transition of tellurene flakes realized by delivering vaporized Te into the tight space between substrates, with time and temperature. The light gray spheres, rods, and flakes represent Te atoms, nano-wires, and thin tellurene flakes, respectively. (c) 3D illustration of the atomic structure of a tellurene nano-flake. (d) Atomic force microscopic (AFM) image of a representative tellurene flake with a thickness of 17.5 nm, where the height profile is extracted along the white dashed line. (e) Thickness statistics of tellurene flakes synthesized by our illustrated method, where 15 to 25 nm thick flakes account for approximately 31% of the total tellurene yield.

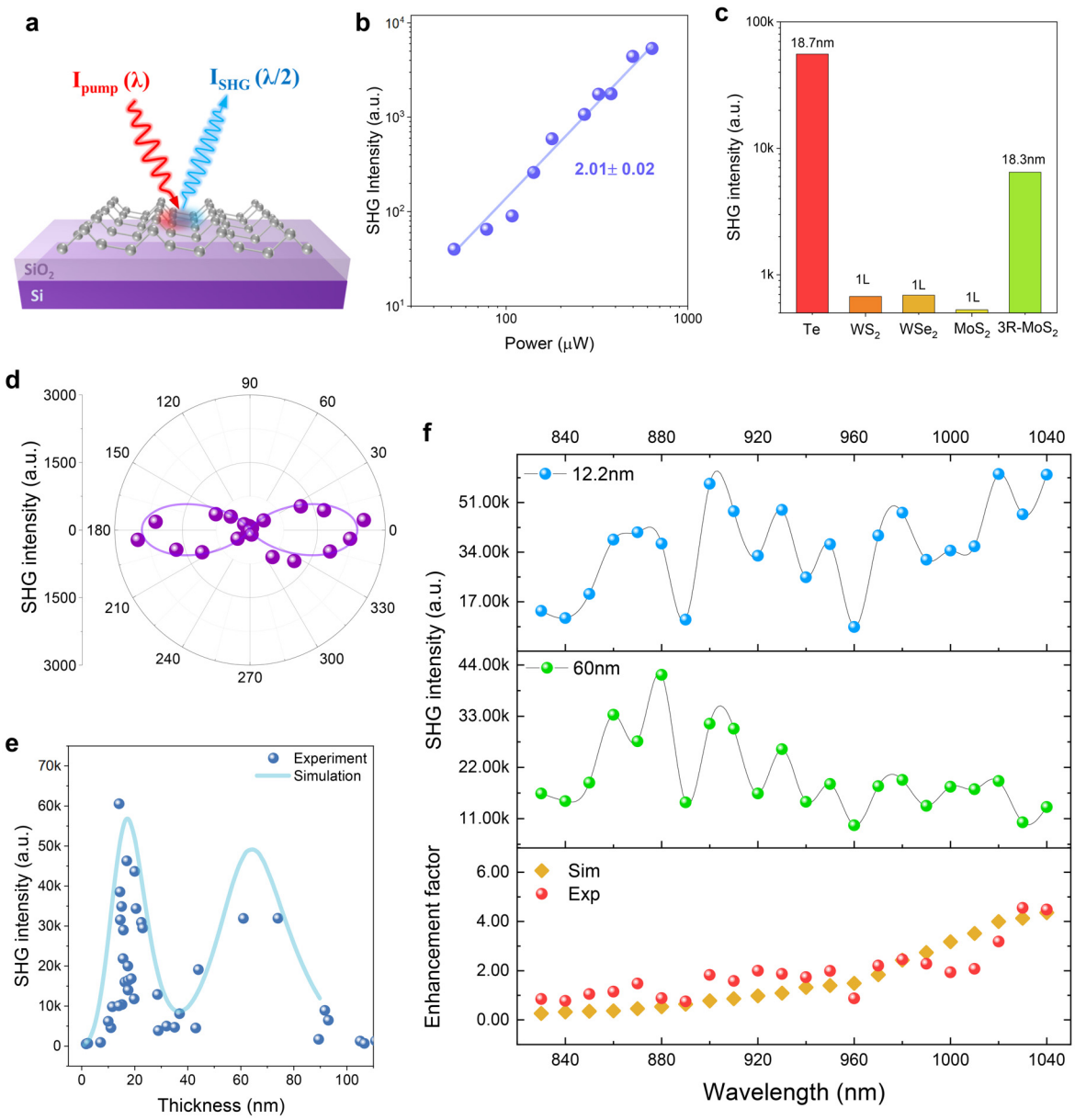

FIG. 2. Characterization of second harmonic generation (SHG) in tellurene flakes. (a) Schematic illustration of SHG mechanism in a 2D tellurene flake, wherein a pump laser reflects the surface at double the frequency and half the wavelength. (b) Power dependence of the SHG signal with both axes presented in logarithmic scale. The spheres represent the measured values, while the solid line indicates the linear fit with a slope of 2.01. (c) Comparison of SHG emission from a tellurene flake and several monolayer transition metal dichalcogenide flakes under 900 nm illumination and the 3 R-MoS_2 with similar thickness. (d) Polar plot of angle resolved SHG. (e) Analytical (blue solid line) and experimental data (blue solid dots) for SHG emission vs tellurene thickness, ranging from 10 to 90 nm, under an excitation wavelength of 900 nm. (f) SHG measurement conducted on two flakes having thicknesses of 12.2 and 60 nm under varied excitation wavelengths, ranging from 830 to 1040 nm. The enhancement curve suggests two flakes with different thickness show consistent response at different wavelengths but with different trends.

Additionally, the existence of lone-pair electrons is conducive to generating induced dipole oscillations in response to optical electric fields, thus leading to large SHG effects.[36,51] The nonlinear anisotropic response was also investigated by employing a polarization-dependent experimental setup to examine the angle-dependent SHG response of the tellurene flake under parallel configuration. As depicted in the polar plot [Fig. 2(d)], the SHG intensity displayed a two-lobe symmetry, indicating the obvious dependence on the angle (θ) between the polarization of incident light and the orientation of the crystal lattice. Specifically, a maximum and minimum SHG response was observed

along the crystal direction [1210] and [0001], respectively, when the sample was rotated, and the orientation of the sample was perpendicular and parallel to the polarized incident light. This distinctive anisotropic behavior could be attributed to the five non-zero and only two independent second-order NLO susceptibility elements induced by poor crystalline symmetry (D_3^4),[36] which is corroborated by the well-fitted curve derived by the analytical solution (supplementary material Note 3). Notably, 2D form of Te does not differentiate the anisotropic behavior compared with the observation in 1D nanowires,[45] owing to the shared crystalline structure of triple helix chains present in both forms.

Flake thickness also substantially influences the SHG emission as demonstrated in Fig. 2(e), which depicts the extracted SHG intensity from thicker tellurene flakes spanning a thickness range from 4 to 90 nm, all measured at a wavelength of 900 nm. When the sample thickness is between 17 nm to approximately 30 nm, there is a distinct decrease in SHG, followed by an increase and decline in SHG intensities associated with the thicker flakes [Fig. 2(e)]. This variation is also observed in the tapered-face sample, where robust emission is apparent across regions with a thickness of less than 20 nm, and the strongest local emission is centered around a thickness of 17 nm (Fig. S7). This behavior can be mainly attributed to two aspects, which are the varying absorption for the pump light wavelength and the light interference arisen within the flake. First, a linear optical reflection and transmission measurement reveals that the thicker Te flake exhibits high absorption ability for pump light in the NIR range (Fig. S5), which indicates that the less portion of pump light can be converted into double frequency output light. This is further supported by the results obtained from the transmission SHG measurements, as the strong forward SHG intensity observed in the thinner regions of the flake diminishes as the flake's thickness increases to larger values, as shown in Fig. S8. Meanwhile, the backward SHG behavior of the Te flake on the transparent substrate also exhibits a similar variation with thickness. This fact can be explained by the correlation between flake thickness and pump light wavelength. Specifically, when the Te flake is exposed to the pump light, the thinner Te flake causes the interference of the fundamental and SHG waves within substrate that serves as the Fabry–Pérot cavity, reaching its maximum SHG when the thickness is around 17 nm. If the thickness keeps increasing, bulk nonlinear coefficient and surface interface will dominate the emission process. The normal incident light reflects, bounces back, and travels forth between two interfaces (Te–air and Te–substrate), resulting in a strong interference effect among the upwardly reflected lights. The round trip phase of the fundamental wave inside the Te flake can thus lead to either weaker light–matter interaction and reduced SHG intensity or constructive interference that enhances the overall SHG signal (Fig. S9). The finite-difference time domain (FDTD) simulation model (supplementary material Note 4) was employed to provide a numerical solution and reaffirm the trend of experimental data regarding the varying flake thickness under the excitation of a 900 nm source and other wavelengths (Fig. S10). To investigate the influence of wavelength on SHG behavior for different thickness flakes, two different flakes having a thickness of 12.2 and 60 nm were measured under increasing excitation wavelengths, ranging from 830 nm to 1040 nm [Fig. 2(f)]. The 12.2 nm thick flake exhibited the strongest emission at an excitation wavelength of 1040 nm and experienced an overall increasing trend with increased wavelength. On the other hand, for another flake with 60 nm thickness, the largest emission was observed at a wavelength of 870 nm, and the overall emission would decrease with a longer wavelength. A comparison between the SHG response of the 12.2 nm flake divided by the SHG response of the 60 nm thick flake response revealed an increasing trend (denoted as the enhancement factor), where the shared second-order nonlinear optical susceptibility of tellurene results in consistent responses at given excitation wavelengths, but the thickness effect results in differing SHG magnitudes. Due to the fact that tellurium becomes very absorptive around this wavelength range,[36] a thicker flake does not possess a stronger light–matter interaction for an enhanced SHG signal. As can be shown in FDTD simulation, the pump light gets reflected or absorbed before it reaches the deeper part of the flake; thus, the SHG only happens strongly near the surface (Fig. S9, supplementary material Note 4). This also emphasizes the importance of selecting an appropriate thickness for Te flakes in nonlinear optical device applications.

Given that the proper thickness of a tellurene flake is an important factor in optimizing the nonlinear optical performance, an effective method for modulating the flake thickness can further influence the application prospects and value of 2D tellurene. Herein, hydrogen (H^+) plasma was employed in this work as a post-growth treatment process to systematically etch and reduce tellurene flake thickness. A similar approach was previously demonstrated to fabricate few layered BP.[52] When the H^+ plasma treatment process starts, H^+ collide and uniformly distribute on the top surface of the thick Te flakes, accordingly, continuously accelerated H^+ react with the surface Te atoms and form H_2Te gas. As H_2Te gas has thermal instability and can ultimately decompose into H_2 and Te at room temperature,[53] this etching method effectively realizes the controllable removal of undesired molecules, thus reducing the thickness of the flakes [Fig. 3(a)]. Due to the dynamic equilibrium state of the reaction between H^+ and Te during the treatment process, thickness modulation provides a reliable etching rate and homogeneity, as confirmed by characterization tests conducted prior to and after the treatment (Fig. S11). As illustrated in Fig. 3(b), through monitoring every etching treatment, the same treatment duration produces a comparable etched thickness, leading to an overall removal rate with a linear relationship between the etched depth and treatment duration. At the same time, to ensure the nonlinear optical properties of treated flakes, the crystallization and purity were examined by Raman tests after each treatment. The spectra clearly showed three separate Raman active modes, and the sharp peaks suggest the high crystal clarity of the Te flakes following the thinning down process [Fig. 3(c)]. A significant blue shift for the E_2 and A_1 modes can be observed when the flake thickness was reduced, because of hardened vibration modes induced by the modulation of interchain and intrachain interactions.[20,54,55] This corresponds well with the results of untreated flakes (Fig. S1) in previous reports.[20,56] Considering the safety concerns associated with the use of Te, monoelemental Te and hydrogen gas can be efficiently separated and collected following the decomposition of H_2Te using techniques such as membrane gas separation and cryogenic distillation based on the distinct physical properties of solid Te and gaseous H_2. To further minimize the risks, encapsulation engineering provides an effective strategy to isolate Te flakes during its use, although it is thermodynamically stable.[16,57,58] For instance, Te flakes can be securely sealed within van der Waals (vdW) layered materials, which offer excellent gas impermeability, mechanical properties, and stability.[59,60] Additionally, the recycling

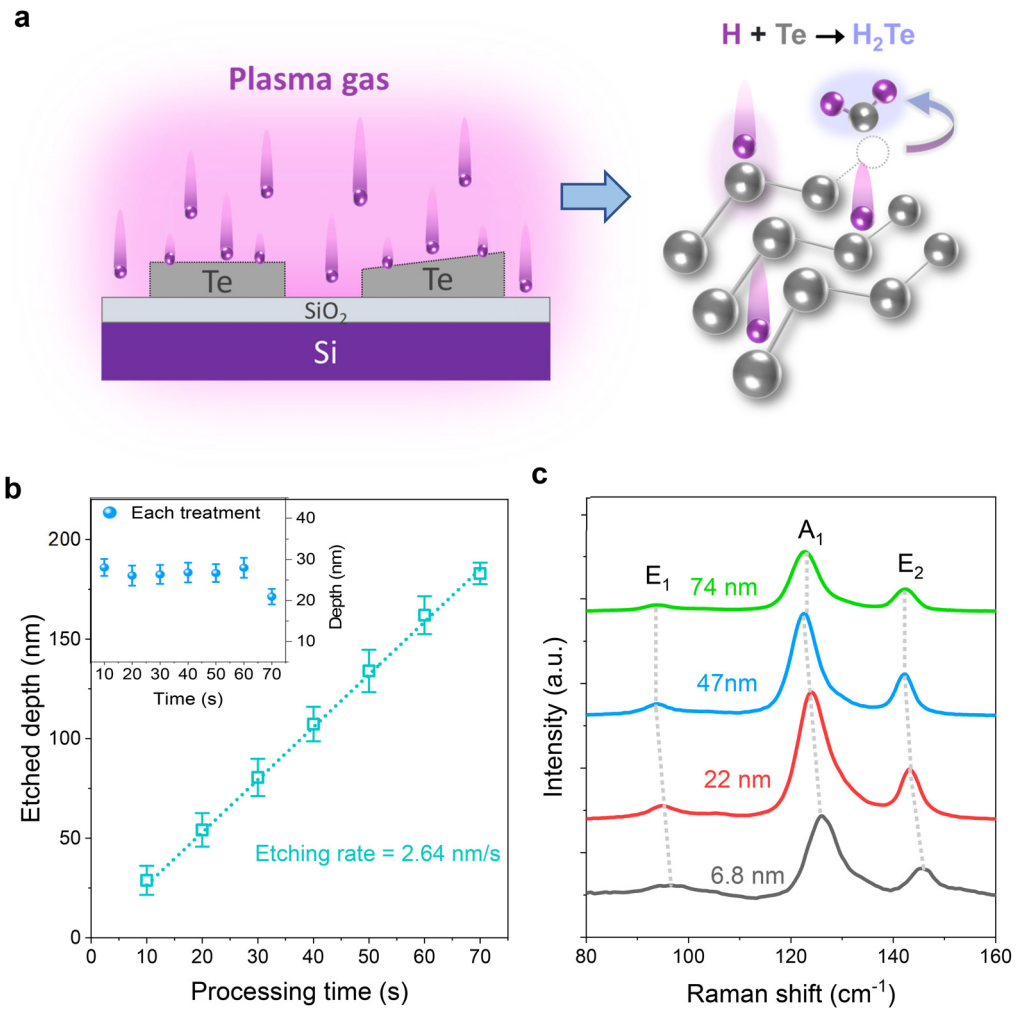

FIG. 3. Investigation of post-growth thinning process of tellurene flakes via hydrogen plasma. (a) Schematic illustration of plasma-assisted post-growth thinning process employed on tellurene flakes, with the thinning process based on the reaction between Te atoms and hydrogen protons in plasma gas. (b) Monitoring thickness change and etching rate from consecutive treatments, where the inset demonstrates the constant etching rate from the average etch thickness of each treatment with tens duration. The error bars represent statistical variation from 10 flakes for each treatment group. (c) Raman spectra of the processed tellurene flake with the thickness decreasing from 74 to 6.8 nm.

and reuse of Te play a critical role in reducing potential harm to both the environment and human health while promoting sustainable resource utilization.

To provide comprehensive insights into the SHG variation induced by the various thickness conditions of treated samples, a treated tapered-face flake serves as a great platform for investigating varying thickness and related SHG behavior [Figs. 4(a) and 4(b)]. After the H^+ treatment, the tapered-face tellurene flake still has high crystallinity and purity, regardless of the thickness change along the length of the flake (Fig. S12). The SHG intensity distribution over the flake surface was imaged under different excitation wavelengths, as presented in Fig. 4(b). As the wavelength increased from 830 to 1040 nm, two strong emission regions with a distinct physical thickness difference had obvious variations in the SHG intensity. When the excitation wavelength was larger than 900 nm, the local emission maximum named 'peak A' had less emission intensity than that of another local maximum "peak B," whose corresponding thickness is around 67 and 17 nm, respectively [Fig. 4(c)]. It is worth noting that even though the treated sample surface is no longer smooth as compared to prior to H^+ etching, the treated flake remains responsive to changes in the excitation wavelength. The positions of the two peaks both exhibited a slight shift toward the thicker region of the flake as the excitation wavelength became longer. For comparison, the FDTD method was utilized to simulate the SHG profiles using the smooth surface obtained from the effective thickness of the treated flake, as depicted in Fig. 4(d). Two emission peaks were observed in the simulation as well. Evidently, these peaks displayed a migration pattern similar to that observed for the treated flake, wherein as the wavelength was altered from 830 to 1040 nm, both peak A and peak B simultaneously move toward the thicker region. After the collection of more

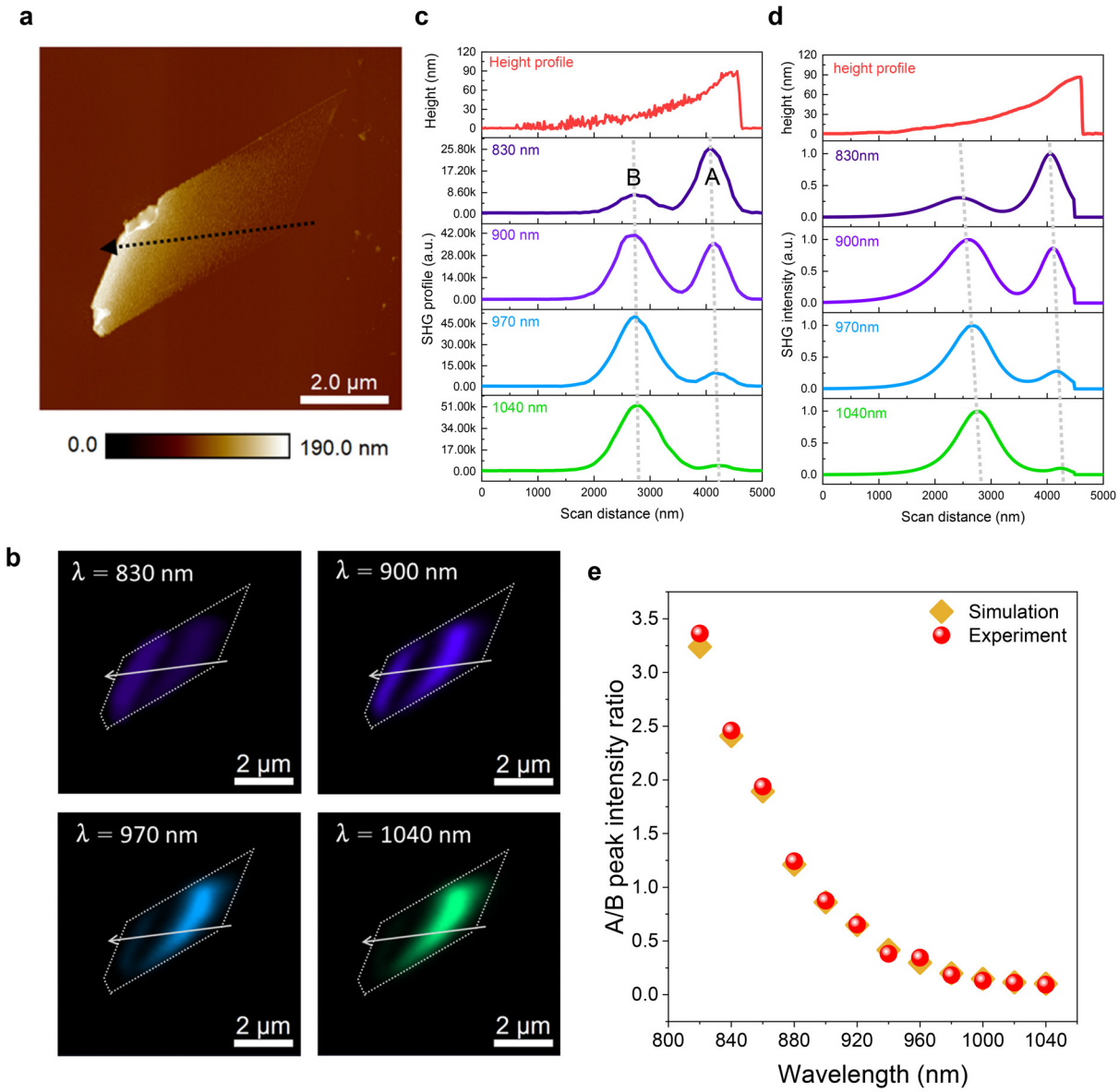

FIG. 4. SHG behavior of tapered tellurene flakes obtained with the post-growth thinning process. (a) AFM image of a tapered-surface tellurene flake after plasma treatment. (b) SHG mapping images of the treated flake shown in (a) under the excitation wavelength at 830, 900, 970, and 1040 nm, where the flake shape has been highlighted by white dot lines. (c) Experimental height profiles and wavelength-dependent SHG intensity profiles extracted along black and white dashed lines in (a) and (b), respectively. (d) Analytical SHG profiles at corresponding wavelengths based on the mean height values of treated surface in (c), where discrepancy in the SHG peak could be attributed to the experimental error introduced during the manual extraction of the profile lines. (e) Comparison of experimental and analytical SHG variation between the local maxima under various wavelengths.

SHG profiles (Fig. S13), the simulated and experimental results exhibit a positive linear relationship between peak location and wavelength, following thickness-dependent behavior. Notably, despite the different root mean square value of roughness (RMS) in the regions of A and B peaks, the larger RMS B peak (3.81 ± 0.11 nm) and smaller RMS A peak (2.65 ± 0.16 nm) both exhibit the same SHG behavior in response to the excitation wavelength. The location of peaks suggests that the roughness does not change the optimized thickness for emission. Meanwhile, comparing the migration distance of peaks between two sets of profiles reveals that the roughened surface of treated samples induced by plasma etching shows no major disparity from the smooth flake, in terms of its thickness-dependent sensitivity to changes in the excitation wavelength. As shown in Fig. 4(e), the ratio of intensities from the two peaks reveals that the treated flake has great agreement with the ratio obtained from simulated results of the smooth flake, further elucidating the thickness-dependent nominal

SHG emission relationship. Therefore, the roughness on the treated flake does not appear to cause deviations of SHG emission induced by light scattering and trapping. Consequently, the corresponding light absorption, phase matching, and light propagation are relatively uninfluenced by the surface roughness during the SHG emission.[61,62] The emission efficiency of a treated flake is equivalent to the optimized performance from the untreated flake of the various thickness under corresponding wavelengths.

In summary, this work provided a comprehensive investigation into the SHG performance of 2D tellurene flakes fabricated by confined space PVD growth, in addition to the SHG performance of the post-process plasma treatment. The tellurene flakes exhibited extraordinary SHG emission and had strong dependence on the flake thickness and excitation wavelength. In addition, the application of plasma treatment effectively reduced flake thickness, enabling tellurene to overcome the limitation of thickness and wavelength interaction. Tellurene's SHG emission is experimentally observed to be about two orders of magnitudes greater than monolayer TMDC counterparts at a larger thickness. This finding offers a fundamental concept to produce all-round 2D tellurium flakes with high SHG emission at various wavelengths. As a result, the thickness engineered tellurene serves as an excellent nano-scaled NLO material, which will find valuable applications in NLO devices, such as electro-optical switches, frequency converters, phase matching, and light signal modulators.

SUPPLEMENTARY MATERIAL

See the supplementary material for the following: Note 1 indicating the sample fabrication and characterization methodology; Note 2 detailing Raman characterization; Note 3 demonstrating the mechanism behind SHG behavior; Note 4 elaborating FDTD simulation for SHG; Figures S1–S3 showing thickness, angle, and temperature-dependent Raman spectra; Fig. S4 comparing the second-order susceptibility among different samples; Figs. S5–S6 exhibiting transmission, reflection, and absorption spectra and extracted refractive indices; Figs. S7–S8 presenting thickness-dependent SHG in reflection and transmission modes; Fig. S9 showing electric field in SHG simulation; Figs. S10–13 showing Raman and SHG results after the treatment; and Fig. S14 illustrating the SHG measurement setup.

ACKNOWLEDGMENTS

The authors acknowledge funding support from ANU Ph.D. student scholarship, Australian Research Council (ARC; Grant Nos. DP220102219, DP240101011, LE200100032) and ARC Centre of Excellence in Quantum Computation and Communication Technology (Grant No. CE170100012), and National Heart Foundation (ARIES ID: 35852). B. L. would like to acknowledge the support from Centre of Advanced Microscopy (CAM), Australian National University.

AUTHOR DECLARATIONS

Conflict of Interest

The authors have no conflicts to disclose.

Author Contributions

Boqing Liu: Conceptualization (equal); Methodology (equal); Writing – original draft (equal); Writing – review & editing (equal). **Zongfu Yu:** Supervision (supporting). **Yuerui Lu:** Conceptualization (equal); Supervision (equal); Writing – review & editing (equal). **Kun Liang:** Conceptualization (equal); Methodology (equal); Writing – original draft (supporting). **Qingyi Zhou:** Investigation (supporting); Methodology (equal); Writing – original draft (supporting); Writing – review & editing (supporting). **Ahmed Raza Khan:** Investigation (supporting); Writing – original draft (supporting). **zhuoyuan Lu:** Investigation (supporting). **Tanju Yildirim:** Writing – original draft (supporting). **Xueqian Sun:** Investigation (supporting). **Sharidya Rahman:** Investigation (supporting). **Yun Liu:** Supervision (supporting); Writing – review & editing (supporting).

DATA AVAILABILITY

The data that support the findings of this study are available from the corresponding author upon reasonable request.

REFERENCES

[1]W.-L. Li, Q. Chen, W.-J. Tian, H. Bai, Y.-F. Zhao, H.-S. Hu, J. Li, H.-J. Zhai, S.-D. Li, and L.-S. Wang, J. Am. Chem. Soc. **136**(35), 12257–12260 (2014).
[2]L. Tao, E. Cinquanta, D. Chiappe, C. Grazianetti, M. Fanciulli, M. Dubey, A. Molle, and D. Akinwande, Nat. Nanotechnol. **10**(3), 227–231 (2015).
[3]Z. Ni, Q. Liu, K. Tang, J. Zheng, J. Zhou, R. Qin, Z. Gao, D. Yu, and J. Lu, Nano Lett. **12**(1), 113–118 (2012).
[4]H. Liu, A. T. Neal, Z. Zhu, Z. Luo, X. Xu, D. Tománek, and P. D. Ye, ACS Nano **8**(4), 4033–4041 (2014).
[5]S. Zhang, Z. Yan, Y. Li, Z. Chen, and H. Zeng, Angew. Chem. **127**(10), 3155–3158 (2015).
[6]A. J. Mannix, B. Kiraly, M. C. Hersam, and N. P. Guisinger, Nat. Rev. Chem. **1**(2), 1–14 (2017).
[7]Z. Zhu, X. Cai, S. Yi, J. Chen, Y. Dai, C. Niu, Z. Guo, M. Xie, F. Liu, J.-H. Cho, Y. Jia, and Z. Zhang, Phys. Rev. Lett. **119**(10), 106101 (2017).
[8]X. Huang, J. Guan, Z. Lin, B. Liu, S. Xing, W. Wang, and J. Guo, Nano Lett. **17**(8), 4619–4623 (2017).
[9]Y.-J. Zhu, W.-W. Wang, R.-J. Qi, and X.-L. Hu, Angew. Chem. Int. Ed. **43**(11), 1410–1414 (2004).
[10]V. E. Bottom, Science **115**(2995), 570–571 (1952).
[11]J.-W. Liu, J.-H. Zhu, C.-L. Zhang, H.-W. Liang, and S.-H. Yu, J. Am. Chem. Soc. **132**(26), 8945–8952 (2010).
[12]H. Peng, N. Kioussis, and G. J. Snyder, Phys. Rev. B **89**(19), 195206 (2014).
[13]J. P. Hermann, G. Quentin, and J. M. Thuillier, Solid State Commun. **7**(1), 161–163 (1969).
[14]X. Cai, X. Han, C. Zhao, C. Niu, and Y. Jia, J. Semicond. **41**(8), 081002 (2020).
[15]G. Zhou, R. Addou, Q. Wang, S. Honari, C. R. Cormier, L. Cheng, R. Yue, C. M. Smyth, A. Laturia, J. Kim, W. G. Vandenberghe, M. J. Kim, R. M. Wallace, and C. L. Hinkle, Adv. Mater. **30**(36), 1803109 (2018).
[16]W. Wu, G. Qiu, Y. Wang, R. Wang, and P. Ye, Chem. Soc. Rev. **47**(19), 7203–7212 (2018).
[17]Z. Gao, F. Tao, and J. Ren, Nanoscale **10**(27), 12997–13003 (2018).
[18]Z. Shi, R. Cao, K. Khan, A. K. Tareen, X. Liu, W. Liang, Y. Zhang, C. Ma, Z. Guo, X. Luo, and H. Zhang, Nanomicro. Lett. **12**(1), 99 (2020).
[19]J. Yang, R. Xu, J. Pei, Y. W. Myint, F. Wang, Z. Wang, S. Zhang, Z. Yu, and Y. Lu, Light. Sci. Appl. **4**(7), e312–e312 (2015).
[20]Y. Wang, G. Qiu, R. Wang, S. Huang, Q. Wang, Y. Liu, Y. Du, W. A. Goddard, M. J. Kim, X. Xu, P. D. Ye, and W. Wu, Nat. Electron. **1**(4), 228–236 (2018).
[21]G. Qiu, S. Huang, M. Segovia, P. K. Venuthurumilli, Y. Wang, W. Wu, X. Xu, and P. D. Ye, Nano Lett. **19**(3), 1955–1962 (2019).
[22]G. Qiu, Y. Wang, Y. Nie, Y. Zheng, K. Cho, W. Wu, and P. D. Ye, Nano Lett. **18**(9), 5760–5767 (2018).
[23]M. Amani, C. Tan, G. Zhang, C. Zhao, J. Bullock, X. Song, H. Kim, V. R. Shrestha, Y. Gao, K. B. Crozier, M. Scott, and A. Javey, ACS Nano **12**(7), 7253–7263 (2018).

[24]M. Peng, R. Xie, Z. Wang, P. Wang, F. Wang, H. Ge, Y. Wang, F. Zhong, P. Wu, J. Ye, Q. Li, L. Zhang, X. Ge, Y. Ye, Y. Lei, W. Jiang, Z. Hu, F. Wu, X. Zhou, J. Miao, J. Wang, H. Yan, C. Shan, J. Dai, C. Chen, X. Chen, W. Lu, and W. Hu, Sci. Adv. **7**(16), eabf7358 (2021).
[25]S. Deckoff-Jones, Y. Wang, H. Lin, W. Wu, and J. Hu, ACS Photonics **6**(7), 1632–1638 (2019).
[26]F. Zhang, G. Liu, Z. Wang, T. Tang, X. Wang, C. Wang, S. Fu, F. Xing, K. Han, and X. Xu, Nanoscale **11**(36), 17058–17064 (2019).
[27]L. Wu, W. Huang, Y. Wang, J. Zhao, D. Ma, Y. Xiang, J. Li, J. S. Ponraj, S. C. Dhanabalan, and H. Zhang, Adv. Funct. Mater. **29**(4), 1806346 (2019).
[28]V. Kumar, N. Coluccelli, and D. Polli, in *Molecular and Laser Spectroscopy*, edited by V. P. Gupta (Elsevier, 2018), pp. 87–115.
[29]A. Autere, H. Jussila, Y. Dai, Y. Wang, H. Lipsanen, and Z. Sun, Adv. Mater. **30**(24), e1705963 (2018).
[30]H. Chen, V. Corboliou, A. S. Solntsev, D.-Y. Choi, M. A. Vincenti, D. de Ceglia, C. de Angelis, Y. Lu, and D. N. Neshev, Light. Sci. Appl. **6**(10), e17060–e17060 (2017).
[31]A. R. Khan, L. Zhang, K. Ishfaq, A. Ikram, T. Yildrim, B. Liu, S. Rahman, and Y. Lu, Adv. Funct. Mater. **32**(3), 2105259 (2021).
[32]B. Liu, T. Yildirim, E. Blundo, D. deCeglia, A. Khan, Z. Yin, H. Nguyen, G. Pettinari, M. Felici, A. Polimeni, and Y. Lu, Appl. Phys. Rev. **10**(2), 021414 (2023).
[33]X. Zhou, J. Cheng, Y. Zhou, T. Cao, H. Hong, Z. Liao, S. Wu, H. Peng, K. Liu, and D. Yu, J. Am. Chem. Soc. **137**(25), 7994–7997 (2015).
[34]I. Abdelwahab, B. Tilmann, Y. Wu, D. Giovanni, I. Verzhbitskiy, M. Zhu, R. Berté, F. Xuan, L. D. S. Menezes, G. Eda, T. C. Sum, S. Y. Quek, S. A. Maier, and K. P. Loh, Nat. Photonics **16**(9), 644–650 (2022).
[35]A. Apte, S. Kouser, F. Safi Samghabadi, L. Chang, L. M. Sassi, D. Litvinov, B. I. Yakobson, A. B. Puthirath, and P. M. Ajayan, Mater. Today **44**, 40–47 (2021).
[36]M. Cheng, S. Wu, Z.-Z. Zhu, and G.-Y. Guo, Phys. Rev. B **100**(3), 035202 (2019).
[37]M. Cheng, Z.-Z. Zhu, and G.-Y. Guo, Phys. Rev. B **103**(24), 245415 (2021).
[38]Q. Wang, M. Safdar, K. Xu, M. Mirza, Z. Wang, and J. He, ACS Nano **8**(7), 7497–7505 (2014).
[39]H. Liu, R. Wu, M. D. Hossain, X. Guo, J. Pan, R. Li, I. H. Abidi, Z. Liu, Y. Zhu, Z. Luo, and Y. Ding, Carbon **173**, 54–60 (2021).
[40]C.-C. Chen, C.-J. Kuo, C.-D. Liao, C.-F. Chang, C.-A. Tseng, C.-R. Liu, and Y.-T. Chen, Chem. Mater. **27**(18), 6249–6258 (2015).
[41]L. Li, J. Liu, M. Zeng, and L. Fu, Nano Res. **14**(6), 1609–1624 (2021).
[42]X. Zhao, J. Shi, Q. Yin, Z. Dong, Y. Zhang, L. Kang, Q. Yu, C. Chen, J. Li, X. Liu, and K. Zhang, iScience **25**(1), 103594 (2022).
[43]S. Sen, U. M. Bhatta, V. Kumar, K. P. Muthe, S. Bhattacharya, S. K. Gupta, and J. V. Yakhmi, Cryst. Growth Des. **8**(1), 238–242 (2008).
[44]C. Wang, P. Wang, S. Chen, W. Wen, W. Xiong, Z. Liu, Y. Liu, J. He, and Y. Wang, ACS Appl. Nano Mater. **5**(2), 1767–1774 (2022).
[45]X. Gan, J. Li, M. Xu, X. Wang, Z. Liu, and J. Zhao, Adv. Opt. Mater. **8**(24), 2001273 (2020).
[46]J. Shi, P. Yu, F. Liu, P. He, R. Wang, L. Qin, J. Zhou, X. Li, J. Zhou, X. Sui, S. Zhang, Y. Zhang, Q. Zhang, T. C. Sum, X. Qiu, Z. Liu, and X. Liu, Adv. Mater. **29**(30), 1701486 (2017).
[47]A. R. Khan, B. Liu, T. Lu, L. Zhang, A. Sharma, Y. Zhu, W. Ma, and Y. Lu, ACS Nano **14**(11), 15806–15815 (2020).
[48]N. Kumar, S. Najmaei, Q. Cui, F. Ceballos, P. M. Ajayan, J. Lou, and H. Zhao, Phys. Rev. B **87**(16), 161403 (2013).
[49]J. Ingers, K. Maschke, and S. Proennecke, Phys. Rev. B **37**(11), 6105–6112 (1988).
[50]J.-H. Song, A. J. Freeman, T. K. Bera, I. Chung, and M. G. Kanatzidis, Phys. Rev. B **79**(24), 245203 (2009).
[51]A. Cammarata, W. Zhang, P. S. Halasyamani, and J. M. Rondinelli, Chem. Mater. **26**(19), 5773–5781 (2014).
[52]J. Pei, X. Gai, J. Yang, X. Wang, Z. Yu, D. Y. Choi, B. Luther-Davies, and Y. Lu, Nat. Commun. **7**, 10450 (2016).
[53]D. C. Dittmer, *Encyclopedia of Reagents for Organic Synthesis* (Wiley, 2001).
[54]A. S. Pine and G. Dresselhaus, Phys. Rev. B **4**(2), 356–371 (1971).
[55]G. Rao, H. Fang, T. Zhou, C. Zhao, N. Shang, J. Huang, Y. Liu, X. Du, P. Li, X. Jian, L. Ma, J. Wang, K. Liu, J. Wu, X. Wang, and J. Xiong, Adv. Mater. **34**(35), 2204697 (2022).
[56]D.-Q. Yang, L.-Q. Zhu, J.-L. Wang, W. Xia, J.-Z. Zhang, K. Jiang, L.-Y. Shang, Y.-W. Li, and Z.-G. Hu, Phys. Status Solidi (b) **259**(7), 2100625 (2022).
[57]J. Singh, P. Jamdagni, M. Jakhar, and A. Kumar, Phys. Chem. Chem. Phys. **22**(10), 5749–5755 (2020).
[58]X. Tai, Q. Zhao, Y. Chen, H. Jiao, S. Wu, D. Zhou, X. Huang, K. Xiong, T. Lin, X. Meng, X. Wang, H. Shen, J. Chu, and J. Wang, Appl. Phys. Lett. **125**(6), 62103 (2024).
[59]B. Liu, T. Yildirim, T. Lü, E. Blundo, L. Wang, L. Jiang, H. Zou, L. Zhang, H. Zhao, and Z. Yin, Nat. Commun. **14**(1), 1050 (2023).
[60]E. Blundo, M. Felici, T. Yildirim, G. Pettinari, D. Tedeschi, A. Miriametro, B. Liu, W. Ma, Y. Lu, and A. Polimeni, Phys. Rev. Res. **2**(1), 12024 (2020).
[61]O. M. Matos, G. A. Torchia, P. Vaveliuk, G. M. Bilmes, and J. O. Tocho, J. Opt. A: Pure Appl. Opt. **4**(2), 130 (2002).
[62]J.-S. Li, Y. Tang, Z.-T. Li, X.-R. Ding, and Z. Li, Appl. Surf. Sci. **410**, 60–69 (2017).